




Evolution of optical phonon modes and thermoelectric properties in doped Bi_2Te_3 : A temperature-dependent Raman spectroscopy study

Minati Tiadi ^{1,2} Dillip K. Satapathy ^{2,*} and Manjusha Battabyal ^{1,†}

¹International Advanced Research Centre for Powder Metallurgy and New Materials (ARCI), IIT M Research Park, Chennai-600113, India

²Soft Materials Laboratory, Department of Physics, Indian Institute of Technology Madras, Chennai-600036, India



(Received 21 October 2022; accepted 6 January 2023; published 20 January 2023)

Due to its three-dimensional bulk-insulating nature and better room-temperature thermoelectric properties, Bi_2Te_3 is widely explored as potential thermoelectric material and topological insulator. Here, we report the effect of smaller atoms (Ge, Se) doping on the evolution of the temperature-dependent optical phonon modes in polycrystalline single-phase Bi_2Te_3 . While undoped Bi_2Te_3 exhibits crystal inversion symmetry lowering in the investigated temperature range, the doped Bi_2Te_3 retains the inversion symmetry below 270 K. As a result, the IR-active A_{1u}^2 phonon mode, which arises due to the lowering of crystal inversion symmetry, disappears in the doped Bi_2Te_3 below 270 K. The increase in the full width at half maxima of Raman peaks and reduction in the phonon lifetime with an increase in temperature confirm the optical phonon decay in doped Bi_2Te_3 , and hence lattice thermal conductivity is expected to decrease at higher temperatures. The lattice thermal conductivity estimated from the optical phonon modes is in line with the experimentally measured value, which affirms that optical phonon vibrations dominate the lattice thermal conductivity of Bi_2Te_3 . At low temperature, the Ge-Se codoped Bi_2Te_3 shows a fourfold enhancement of the Seebeck coefficient compared to that of undoped Bi_2Te_3 . Our results give an insight into the optical phonon decay mechanism in the doped Bi_2Te_3 and corroborate that optical phonons play a vital role in the lattice thermal conductivity of polycrystalline Bi_2Te_3 . Also, it is found that Se-Ge codoped Bi_2Te_3 can be used as an efficient near-room temperature thermoelectric material.

DOI: [10.1103/PhysRevMaterials.7.015401](https://doi.org/10.1103/PhysRevMaterials.7.015401)

I. INTRODUCTION

With increasing concern about environmental pollution and the energy crisis, thermoelectric (TE) materials, which can directly convert thermal energy into electrical energy and vice versa, have received considerable attention [1–3]. No noise, nonpollution, and operational reliability are the main advantages of TE devices [3,4]. Finding new green energy production and making existing energy systems more efficient are the major scope of research on TE materials. Among the potential TE materials [5–8], Bi_2Te_3 based compounds are the best candidates for room-temperature TE applications because they possess the highest thermoelectric figure of merit at room temperature [9–12]. Recently, Bi_2Te_3 has also shown potential to be a three-dimensional (3D) topological insulator (TI), a new class of quantum matter with conductive massless Dirac fermions on the surface [9]. The doped Bi_2Te_3 like $\text{Bi}_2\text{Te}_2\text{Se}$ and $\text{Bi}_{1-x}\text{Sb}_x\text{Te}_{2-x}\text{Se}_x$ are researched to enhance their thermoelectric and topological insulating properties [13].

The ternary and quaternary $\text{Bi}_2\text{Te}_2\text{Se}$ alloys, which can be obtained by doping at the Te and Bi sites of Bi_2Te_3 , are widely used in the thermoelectric device applications [14,15]. It is known that polycrystalline bismuth telluride (Bi_2Te_3) is a narrow band gap semiconducting material with an orthorhombic structure comprising five atoms of Te–Bi–Te–Bi–Te thick

covalently bonded stacks/layers [16]. Although single-doped and double-doped/codoped Bi_2Te_3 are widely explored as potential thermoelectric and topological insulating materials, local crystal structure symmetry of these compounds are not investigated in detail. In fact, the bonds in the Te–Bi–Te–Bi–Te layer will be altered in doped Bi_2Te_3 and will vibrate at different frequencies; those will give rise to several optical and acoustic phonon modes. These phonon vibrations play a crucial role in tailoring the TE efficiency (zT) of a material as can be understood from the equation $zT = S^2T/\rho\kappa$, where S , ρ , and κ respectively are Seebeck coefficient, electrical resistivity, and total thermal conductivity of the samples at absolute temperature T [5]. To obtain high zT , it is important to have higher S , low ρ , and κ . κ of a TE system can be lowered by reducing lattice thermal conductivity (κ_{lattice}), as $\kappa = \kappa_e + \kappa_{\text{lattice}}$. In a TE semiconductor, κ_e contributes only 10% to κ . Hence κ_{lattice} dominates the thermal conductivity in a TE material. Two types of phonon modes, namely optical and acoustic phonons, contribute to κ_{lattice} [17]. Although it is trivial that acoustic phonon modes dominate κ_{lattice} owing to their higher group velocity, recent studies show that κ_{lattice} in TE semiconductors can also be estimated from the optical phonon modes [17,18]. So, it is required to understand the temperature dependent optical phonon vibrations in a TE system. The optical phonon modes in a doped polycrystalline Bi_2Te_3 system can be understood by realizing the local symmetry of the Te–Bi–Te–Bi–Te layer when there is doping at the Bi and Te site. The interdependence between the possession of those random sites might give rise to a local inversion-symmetry

*dks@iitm.ac.in

†manjusha.battabyal@gmail.com

lowering/breaking, limiting the topological and thermal properties of this compound. The high-frequency phonon modes obtained in Raman spectroscopy depend on the local crystal lattice symmetry, and hence can be able to estimate the lattice anharmonicity in Bi_2Te_3 [19,20]. Lattice anharmonicity leads to a decay of phonon lifetime and lowers the lattice thermal conductivity of Bi_2Te_3 , which is a crucial parameter for thermoelectric applications. The phonon decay mechanism can be explained by analyzing the peak shift and full width at half maxima of the Raman modes, measured at different temperatures. Thus it is essential to study the optical vibration mechanism in doped polycrystalline Bi_2Te_3 to gain insight into its promising TE efficiency.

In this study, we have investigated the temperature-dependent optical phonon modes of undoped and doped Bi_2Te_3 from 131 to 483 K to see the effect of lighter and smaller Se and Ge atoms doping on the phonon decay mechanism and lattice thermal conductivity of polycrystalline Bi_2Te_3 . It was observed that while undoped Bi_2Te_3 has lattice symmetry lowering in the entire temperature range, Se and Ge doping revives the lattice inversion symmetry in Bi_2Te_3 below 270 K. The phonon lifetime of the samples is found to decrease with an increase in temperature and hence lattice thermal conductivity is expected to degrade at higher temperatures for polycrystalline Bi_2Te_3 . Ge-Se codoping gives rise to threefold increment of the Seebeck coefficient and reduces the lattice thermal conductivity of Bi_2Te_3 . As a result, the TE efficiency of the Se-Ge codoped Bi_2Te_3 is found to be significantly improved near room temperature.

II. EXPERIMENTS

Undoped (Bi_2Te_3), Se-doped ($\text{Bi}_2\text{Te}_{2.8}\text{Se}_{0.2}$), and Se-Ge codoped ($\text{Bi}_{1.95}\text{Ge}_{0.05}\text{Te}_{2.8}\text{Se}_{0.2}$ and $\text{Bi}_{1.90}\text{Ge}_{0.1}\text{Te}_{2.8}\text{Se}_{0.2}$) samples are synthesized using the high temperature melting route. The solid pieces of individual elements (Bi, Te, Se, and Ge) in proper ratio are vacuum sealed in a quartz tube and melted in a furnace (make: M/S Navatherm, Germany) at 1073 K. Next, the melted ingots are crushed and ball-milled in a tungsten carbide (WC)-Co jar for 3 h. The resulting powders are compacted using a hot press at 825 K to obtain cylindrical pellets of 20 mm diameter and 4 mm thickness. For the easy reference of the samples, Bi_2Te_3 and $\text{Bi}_2\text{Te}_{2.8}\text{Se}_{0.2}$ will be referred to as undoped and Se-doped Bi_2Te_3 , while $\text{Bi}_{1.95}\text{Ge}_{0.05}\text{Te}_{2.8}\text{Se}_{0.2}$ and $\text{Bi}_{1.90}\text{Ge}_{0.1}\text{Te}_{2.8}\text{Se}_{0.2}$ will be referred to as Se-Ge codoped Bi_2Te_3 in the manuscript. The density of the pellets are measured using Archimedes principle and is found to be about 99% of the theoretical density reported for bulk Bi_2Te_3 samples.

Next, we have probed the crystal symmetry and microstructure of the samples using an x-ray diffractometer (M/S Rigaku, Japan) and scanning electron microscopy (Zeiss SEM with EDAX detector), along with the high resolution transmission electron microscopy (JEOL, JEM-2100plus). The Raman spectroscopy at different temperatures and different laser power are carried out on the hot pressed pellets using the HORIBA LabRAM confocal micro-Raman system equipped with a liquid-nitrogen-cooled CCD camera, as described in our earlier report [17]. The

wavelength of the used laser source is 632 nm and the spot size of the laser beam is $\sim 1 \mu\text{m}$. The optical power of the laser source can be varied from $\sim 0.06 \text{ mW}$ to 5.2 mW. The resolution of the Raman spectra is 1 cm^{-1} . All the Raman spectra were obtained from 80 cm^{-1} to 160 cm^{-1} with 5 s acquisitions time and an 1800 lines per inch grating. While a 100 objective was used for room temperature measurements, a 50 objective was used for temperature dependent Raman measurements. The temperature dependent electrical conductivity, and Seebeck coefficient measurements from 150 K to 375 K are performed on cut cuboidal pieces of the samples having $12 \text{ mm} \times 4 \text{ mm} \times 4 \text{ mm}$ dimensions using ZEM-3 equipment (make: M/S Ulvac Riko, Japan). The thermal conductivity of the samples is carried out from 150 to 320 K using Physical Properties Measurement System (make: Quantum Design, USA).

III. RESULTS AND DISCUSSIONS

Bismuth telluride (Bi_2Te_3) is known to crystallize in a layered structure preserving the rhombohedral symmetry. To confirm this, Bragg diffraction patterns are recorded for the undoped and doped Bi_2Te_3 samples and are shown in Fig. 1(a). The diffraction pattern reveals that the hot pressed samples are of single Bi_2Te_3 phase with a rhombohedral structure having $R\bar{3}m$ space group [21]. To obtain further information about the doping-dependent change in the lattice parameter, the highest intensity peak, i.e., (015) peak for samples with different doping, is shown separately in Fig. 1(b). As can be seen from Fig. 1(b), the (015) peak shifts towards a higher angle for Se- and Ge-doped samples. This suggests a gradual reduction of the lattice parameter in $\text{Bi}_2\text{Te}_{2.8}\text{Se}_{0.2}$, $\text{Bi}_{1.95}\text{Ge}_{0.05}\text{Te}_{2.8}\text{Se}_{0.2}$, and $\text{Bi}_{1.90}\text{Ge}_{0.1}\text{Te}_{2.8}\text{Se}_{0.2}$ samples. Further, the measured XRD profiles are fitted using Rietveld refinement to obtain the crystal symmetry and the lattice spacing and are depicted in Fig. 1(c). The Rietveld refinement of the XRD data is executed using the FULLPROOF program and the Pseudo-Voigt function is chosen for profile refinement. The change in the lattice parameters due to doping is plotted in Fig. 1(d). The crystal symmetry is found to be unaltered due to doping, while a slight decrease in the lattice parameter is observed for the doped Bi_2Te_3 . The lattice parameter decreases due to the incorporation of smaller Se^{2-} (1.83 Å) and Ge^{2+} (0.87 Å) ions at the larger Te^{2-} (2.21 Å) and Bi^{+3} (1.03 Å) sites [22]. The comparatively lower values of the lattice parameters in the doped Bi_2Te_3 are expected to affect the bond strength and lattice vibrations, which are discussed in the later part of the manuscript. The crystallite size estimated from the measured XRD profiles using Scherrer's formula is found to be $\sim 15.57 \pm 1.07 \text{ nm}$ for undoped Bi_2Te_3 . The average crystallite size decreases to $\sim 13.89 \pm 1.32 \text{ nm}$ in Se doped $\text{Bi}_2\text{Te}_{2.8}\text{Se}_{0.2}$ samples. It decreases even further to $\sim 13.65 \pm 1.48$ and $\sim 13.13 \pm 1.46 \text{ nm}$ for $\text{Bi}_{1.95}\text{Ge}_{0.05}\text{Te}_{2.8}\text{Se}_{0.2}$ and $\text{Bi}_{1.90}\text{Ge}_{0.1}\text{Te}_{2.8}\text{Se}_{0.2}$ samples, respectively. The reduction in the crystallite size may be due to the doping-induced enhanced strain in the lattice of the Se-doped and Se-Ge codoped samples [23].

The crystalline properties of the samples are further confirmed from the transmission electron microscopy images, recorded for the Se-doped Bi_2Te_3 sample. The selected area

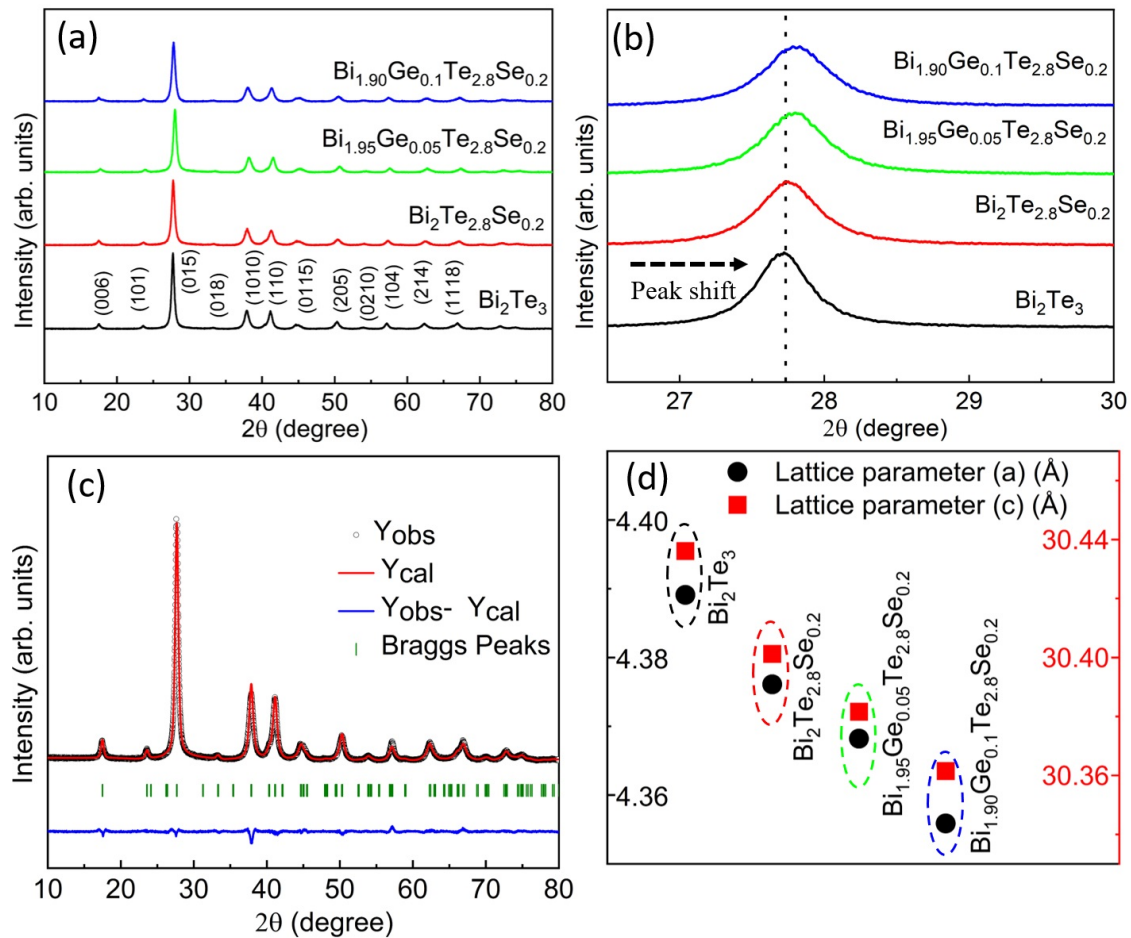


FIG. 1. (a) Measured x-ray diffraction pattern of the undoped and doped Bi_2Te_3 , (b) the magnified view of the (015) peak of the doped and undoped samples showing the shift towards higher Bragg angle, (c) Rietveld refinement of $\text{Bi}_2\text{Te}_{2.8}\text{Se}_{0.2}$ sample, and (d) lattice parameter of the undoped and doped Bi_2Te_3 .

electron diffraction pattern from the $\text{Bi}_2\text{Te}_{2.8}\text{Se}_{0.2}$ sample is shown in the inset in Fig. 2(a). The presence of a set of concentric diffraction rings with distinct sharp bright spots confirms the nanocrystalline nature of the samples. The lattice spacing calculated from the rings are characteristics of the rhombohedral Bi_2Te_3 phase [21,24]. The d spacing calculated for the (2110) plane and (205) plane from the diffraction ring are found to be 1.81 Å, and 1.29 Å, respectively [Fig. 2(b)]. The x-ray diffraction and the transmission electron microscopy data unequivocally confirm that the samples are single phase, crystalline, and have rhombohedral symmetry. Furthermore, scanning electron microscopy reveals the layered morphology of the samples, which is shown in Figs. 2(c) and 2(d). We note that the formation of randomly distributed well-stacked layers is a signature of both doped and undoped Bi_2Te_3 [25]. The stacking of the lamellar structures is found to be randomly distributed throughout the sample spanning over large domains of the order of about $\sim 20 \mu\text{m}$. Overall, the XRD, TEM, and SEM give a signature of nonpreferential growth of Bi_2Te_3 lamella in the samples.

Next, in order to investigate the optical phonon vibrations and the related thermal transport properties, we have carried out the temperature dependent Raman spectroscopy on undoped/binary, Se-doped/ternary, and Ge-Se

codoped/quaternary Bi_2Te_3 samples. Although temperature dependent Raman spectroscopy is reported for single crystal of the quaternary BiSbTeSe_2 system, reports for the polycrystalline ternary and quaternary systems Bi_2Te_3 is scarce [26]. The Raman spectra recorded at 300 K for the undoped and doped samples are depicted in Fig. 3. It shows the presence of three distinct peaks or optical phonon modes for undoped and doped Bi_2Te_3 samples. The appearance of three optical modes can be understood by taking into account the symmetry of the crystal and the associated vibrational modes.

As mentioned earlier, the undoped binary Bi_2Te_3 is a narrow band gap semiconductor having a rhombohedral tetradymite-type crystal structure. A schematic showing a unit cell of Bi_2Te_3 is shown in Fig. 4(a). This unit cell contains 15 atomic lattice planes stacked into three quintuple layers, i.e., five-atom bonded stacks with a sequence, $\text{Te}^1\text{-Bi-Te}^2\text{-Bi-Te}^1$, and marked as “QL” in the unit cell [refer to Fig. 4(a)]. Two types of tellurium atoms, i.e., Te^1 and Te^2 , having different chemical states and five covalently bonded monoatomic hexagonal sheets are also indicated in Fig. 4(a). The quintuples are coupled via the weak van der Waals forces between the $\text{Te}^1\text{-Te}^1$ layers of adjacent quintuples. Moreover, the Bi atoms are sandwiched between Te^1 and Te^2 atoms. It is reported that bulk Bi_2Te_3 crystal has 15 phonon

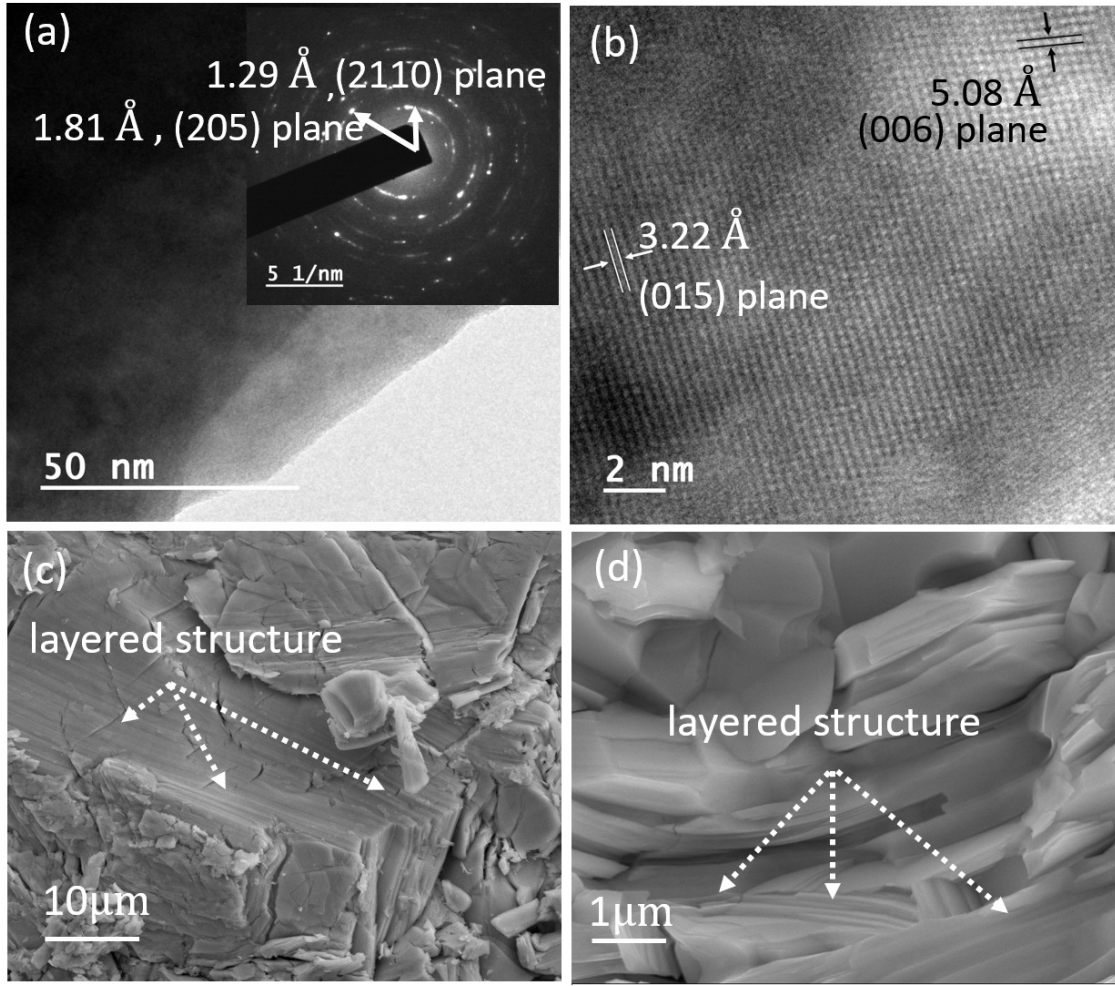


FIG. 2. (a), (b) High resolution TEM image of $\text{Bi}_2\text{Te}_{2.8}\text{Se}_{0.2}$ samples; (c) and (d) represent the SEM image collected from the cleavage surface of undoped Bi_2Te_3 ingot.

polarization branches, out of which three are acoustic modes and the remaining twelve are optical modes [27]. From the group theoretical analysis, it is established that all the 12 optical phonon modes have $2A_{1g}$, $2E_g$, $2A_{1u}$, and $2E_u$ symmetries. The “ E ” and “ A ” denote the in-plane (transverse) and out-of-plane (longitudinal) (C_H axis) lattice vibrations, respectively [27], whereas subscripts “ g ” and “ u ” stand for Raman active and IR-active modes, respectively. Both E_g^1 and A_{1g}^1 appear at lower frequencies than E_g^2 and A_{1g}^2 as the former modes are related to the *in-phase* movement of Bi and the Te^1 , while the latter modes are due to their *out-of-phase* movement. Hence the bond strength between Bi and Te^1 is mainly responsible for the optical phonon modes. For crystals having inversion symmetry like Bi_2Te_3 , the Raman active modes must have even parity and IR-active modes must have odd parity [28]. The odd-parity IR-active phonons do not show up in Raman spectra for bulk polycrystalline samples as long as the inversion symmetry is preserved in the unit cell of the crystal. The higher bond strength between Bi and Te^1 helps in retaining the inversion symmetry in the crystal, while the weakening bond strength between Bi and Te^1 atoms facilitates the inversion symmetry breaking. Further, the bond strength depends on the distance between the atoms and becomes weaker as

the bond length between Bi and Te^1 atoms increases. For the Bi_2Te_3 system, the total optical phonon vibration Γ_{vib} can be written as

$$\Gamma_{\text{vib}} = 2E_g + 2E_u + 2A_{1g} + 2A_{1u}.$$

We note that the transverse modes, i.e., E modes, are having double degeneracy [29]. For Raman active modes, the Raman tensors can be written as [29]

$$A_{1g} = \begin{pmatrix} a & 0 & 0 \\ 0 & a & 0 \\ 0 & 0 & b \end{pmatrix}, \quad E_g^1 = \begin{pmatrix} c & 0 & 0 \\ 0 & -c & d \\ 0 & d & 0 \end{pmatrix},$$

$$E_g^2 = \begin{pmatrix} 0 & -c & -d \\ -c & 0 & 0 \\ -d & 0 & b \end{pmatrix}, \quad (1)$$

where a , b , c , and d are the components of the Raman tensor. The nonzero off-diagonal Raman tensor components in the E_g mode play a vital role in differentiating the E_g mode from the A_{1g} mode.

After discussing the optical phonon modes that can possibly arise in Bi_2Te_3 based compounds, we now discuss the Raman and IR-active modes that are observed in our samples

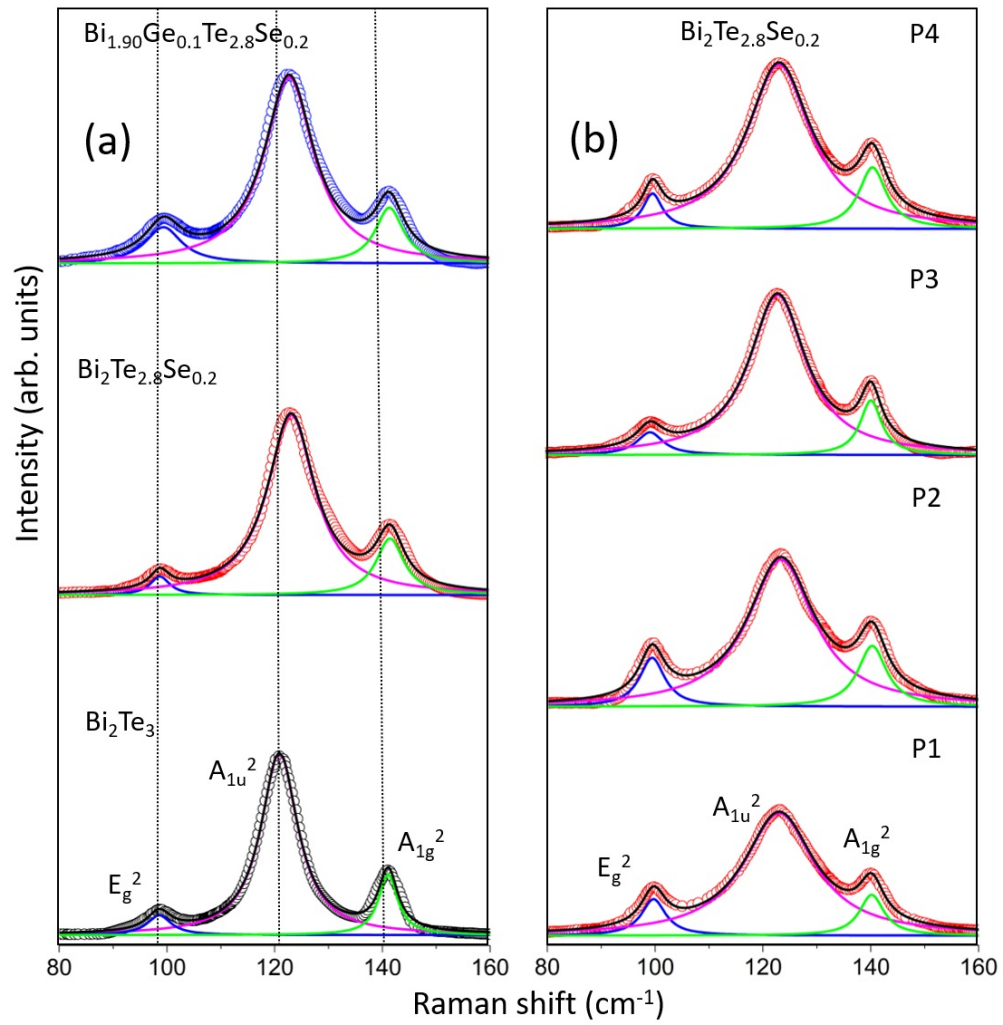


FIG. 3. Raman spectra at 300 K (a) undoped and doped Bi_2Te_3 and (b) on different points of the surface of $\text{Bi}_2\text{Te}_{2.8}\text{Se}_{0.2}$.

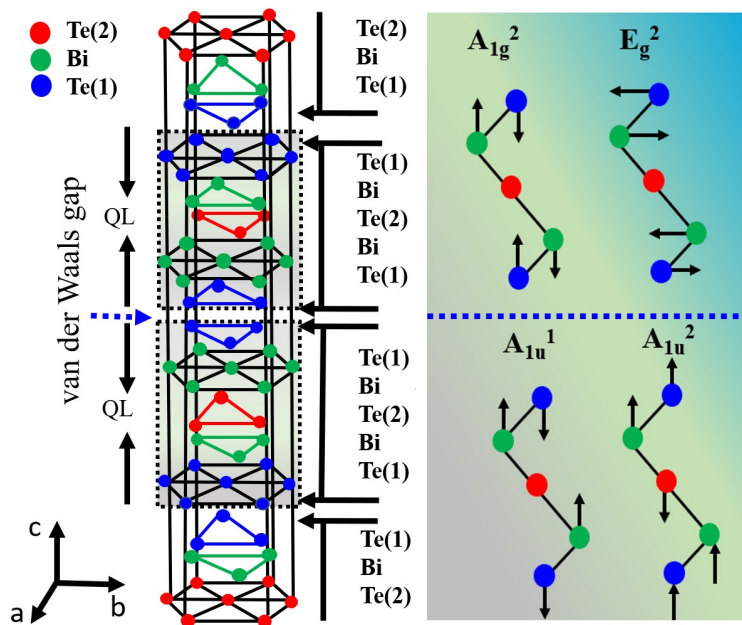


FIG. 4. Left side image shows the schematic of Bi_2Te_3 crystal structure with the quintuple layers and van der Waals gap and the right side image represents the schematic of A_{1g}^2 , E_g^2 , A_{1u}^1 , and A_{1u}^2 optical modes present in Bi_2Te_3 .

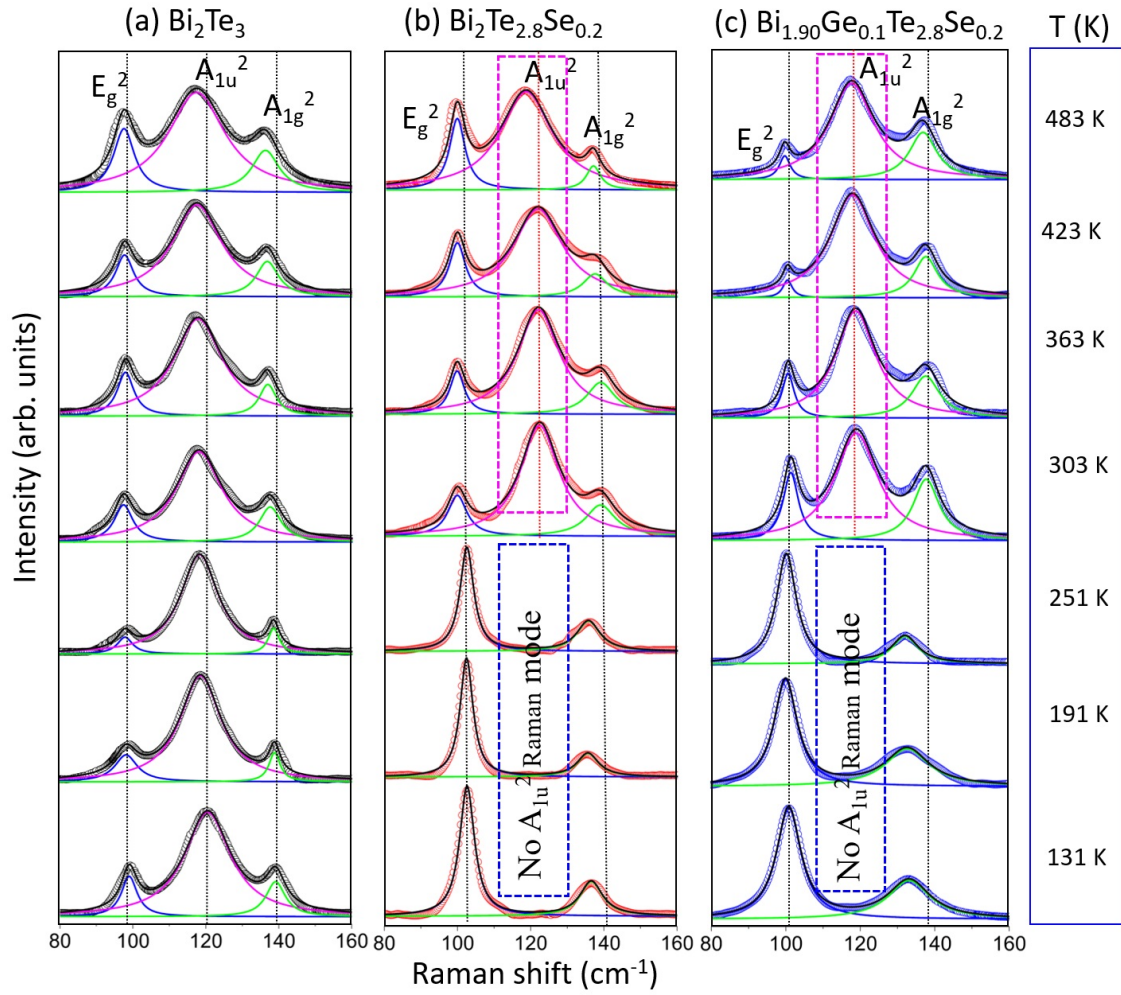


FIG. 5. Temperature dependent Raman spectra of (a) Bi_2Te_3 , (b) $\text{Bi}_2\text{Te}_{2.8}\text{Se}_{0.2}$, and (c) $\text{Bi}_{1.90}\text{Ge}_{0.1}\text{Te}_{2.8}\text{Se}_{0.2}$ from 131 to 483 K. For clarification, the Raman spectra are plotted at the 60 K interval.

in a temperature range of 131 K to 483 K. As depicted in Fig. 3, at 300 K, E_g^2 , A_{1u}^2 , and A_{1g}^2 modes appear at ~ 100 , 120, and 140 cm^{-1} , respectively, and are in line with the reported Raman modes in the literature [30]. The IR-active A_{1u}^2 mode is found to be present in all the samples at 300 K, irrespective of the doping. The appearance of the A_{1u}^2 mode confirms the inversion symmetry breaking/lowering in all the samples at 300 K. The observation of the infrared active A_{1u}^2 phonon mode may be due to strong confinement effects and the loss of local inversion symmetry [25,27,31]. It is germane to note that spatial inhomogeneity and associated local defects, which are usually present in thin films, can also give rise to the A_{1u}^2 peak in the Raman spectra and is investigated in detail [25,30]. To confirm, if there exists any spatial inhomogeneity and/or associated localized surface defects leading to the appearance of the A_{1u}^2 mode, Raman spectra are recorded from different spatial locations on the surface of the sample as marked in the schematic of the sample surface [see Fig. 3(b)]. The Raman spectra recorded at multiple different locations are shown in Fig. 3(b). The measured spectra corresponding to different locations are similar in nature and all the spectra contain three peaks including the IR-active A_{1u}^2 peak. This unambiguously

confirms that the A_{1u}^2 peak, observed at 300 K, is not associated with surface defects; rather it is an intrinsic property of the samples. In other words, the presence of the A_{1u}^2 peak indicates the inversion symmetry breaking in the undoped and doped Bi_2Te_3 samples studied here.

To further investigate the temperature-dependent behavior of Raman and IR-active modes, Raman spectra recorded in the temperature range from 131 K to 483 K with a 60 K interval for undoped and doped samples are shown in Fig. 5. The IR-active A_{1u}^2 mode is found to be present in the undoped sample from 483 K to 131 K, which disappears in doped samples in the low-temperature region, i.e., 131 to 251 K, indicated by the dotted blue rectangular region in Figs. 5(b) and 5(c). To know the exact temperature at which the A_{1u}^2 mode disappears in doped samples, Raman measurements with a temperature step of 5 K were carried out and are shown in Fig. 6. It can be observed from Fig. 6 that the intensity of the A_{1u}^2 mode decreases as the temperature reduces below 283 K and the mode completely disappears at about 273 K.

The absence of the A_{1u}^2 peak in the doped samples at low temperatures suggests the presence of inversion symmetry in the doped Bi_2Te_3 crystals at low temperatures. The inversion

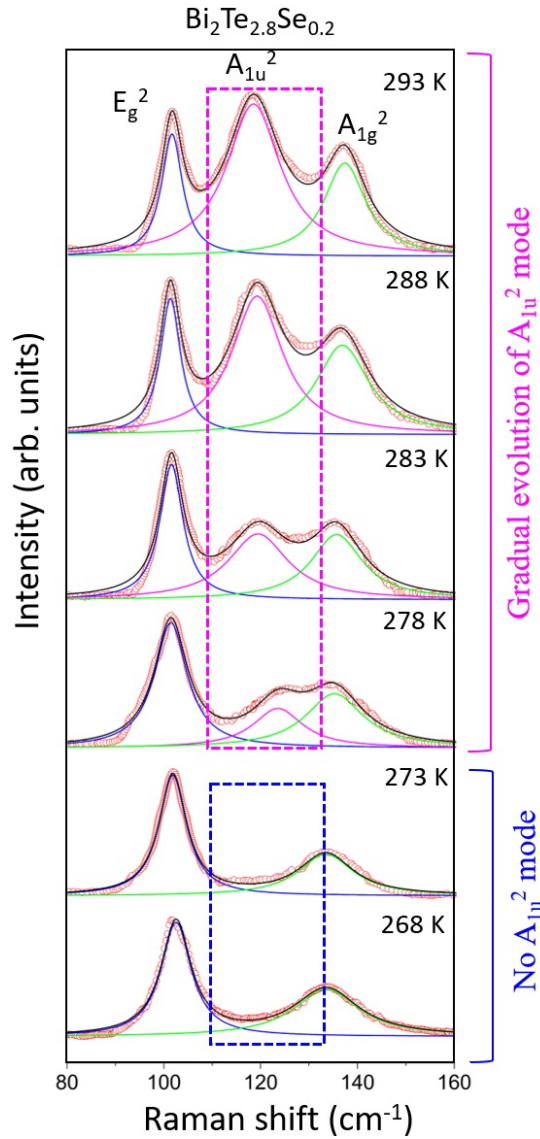


FIG. 6. Raman spectra of $\text{Bi}_2\text{Te}_{2.8}\text{Se}_{0.2}$ from 293 K to 268 K with a 5 K step size to show the disappearance of the A_{1u}^2 peak in the doped sample at low temperature.

symmetry appears to be restored as temperature is lowered in the doped samples. The gradual disappearance of the A_{1u}^2 peak with decrease in temperature also suggests that the inversion symmetry breaking is not an abrupt process. We reiterate that the recovery of inversion symmetry at lower temperatures is

observed only for doped samples. The recovery of the inversion symmetry is possibly associated with the enhanced strength of atomic bonds in the doped samples, which is aided by the doping induced reduction in the lattice constants. As discussed in the XRD section, the lattice parameters of the doped Bi_2Te_3 samples are lower than the undoped sample [Fig. 1(d)]. Taking the room temperature lattice parameter values from the XRD data, and the coefficient of thermal expansion of Bi_2Te_3 from the literature [32], the lattice parameters of the undoped and doped Bi_2Te_3 systems are estimated at 131, 191, 251, and 273 K and are tabulated in Table I. It can be observed from Table I that, at 273 K, the lattice parameters of the doped Bi_2Te_3 are lower than that of the undoped sample, and it decreases further as the temperature goes down to 131 K. The smaller lattice parameters in the doped Bi_2Te_3 at low temperatures lead to the strengthening atomic bonding, which helps in restoring the inversion symmetry for the doped samples below 268 K. We note that, at higher temperatures, both Raman and IR-active peaks are observed irrespective of the doping state of the sample [see Figs. 5(a), 5(b) and 5(c)].

After discussing the interesting features observed in optical phonon modes for the doped Bi_2Te_3 at low temperatures, we now present the temperature evolution of Raman and IR modes. A clear shift of the peak position along with a broadening of the peaks are observed with an increase in temperature from 131 K to 483 K for all the samples and are shown in Fig. 5. For the undoped Bi_2Te_3 , all three peaks, i.e., E_g^2 , A_{1u}^2 , and A_{1g}^2 , shift towards lower wave numbers as the temperature increases. This indicates a reduction of the energy of the optical phonon vibration modes with an increase in the temperature. Moreover, the full width at half maxima (FWHM) of the optical phonon modes increases with the increase in temperature and is in line with the predictions of the “anharmonic phonon coupling model” [20]. This model states that, when the temperature is increased, the lattice anharmonicity allows the mutual interaction between harmonic phonons. This results in a change in the frequency and the FWHM of the Raman peaks [20]. Furthermore, the temperature-induced thermal expansion of the lattice leads to an anharmonic decay of phonons from higher energy to lower energy and directly alters the frequency and FWHM of the phonon modes.

According to He *et al.*, at low temperature, the three phonon decay process contributes to the broadening of the optical phonon peaks, whereas the four phonon decay process dominates at higher temperatures [20]. But there is always a certain possibility that both the mechanisms may

TABLE I. Calculated lattice parameters of undoped and doped Bi_2Te_3 samples in the temperature range of 131 K to 300 K.

T (K)	Bi_2Te_3		$\text{Bi}_2\text{Te}_{2.8}\text{Se}_{0.2}$		$\text{Bi}_{1.9}\text{Ge}_{0.1}\text{Te}_{2.8}\text{Se}_{0.2}$	
	a (Å)	c (Å)	a (Å)	c (Å)	a (Å)	c (Å)
131 K	4.380	30.372	4.367	30.336	4.346	30.297
191 K	4.383	30.394	4.370	30.359	4.353	30.320
251 K	4.386	30.417	4.373	30.382	4.354	30.342
273 K	4.387	30.425	4.374	30.390	4.355	30.350
300 K	4.389 ± 0.005	30.436 ± 0.007	4.376 ± 0.004	30.401 ± 0.007	4.356 ± 0.005	30.361 ± 0.006

TABLE II. Calculated fitting parameters from the Raman spectra of undoped and doped Bi_2Te_3 samples in the temperature range of 131 K to 483 K. Since there is no A_{1u}^2 peak for the doped samples at low temperature, the fitting parameters for A_{1u}^2 peak in the low temperature region is not mentioned in the table.

Sample	E_g^2 peak		A_{1u}^2 peak	A_{1g}^2 peak	
	Low T	High T	High T	Low T	High T
Bi_2Te_3	A = -0.01294 B = 1.46448×10^{-5} C = 0.00241 D = -1.08807×10^{-6}	A = -0.00312 B = 2.08331×10^{-5} C = 0.012126 D = -1.04167×10^{-5}	A = -0.01664 B = 1.59722×10^{-5} C = 0.009581 D = -3.47222×10^{-6}	A = -0.01024 B = 9.57543×10^{-6} C = 0.01004 D = -6.25356×10^{-6}	A = -0.0154 B = 1.11111×10^{-5} C = 0.03219 D = -2.43056×10^{-5}
$\text{Se}_{0.2}$	A = -0.00933 B = 1.48811×10^{-5} C = 0.00241 D = -1.408807×10^{-6}	A = -0.00353 B = 6.94444×10^{-7} C = 0.00813 D = -5.5556×10^{-6}	A = -0.01913 B = 2.73123×10^{-7} C = 0.03008 D = -8.333×10^{-6}	A = -0.01346 B = 3.53861×10^{-6} C = 0.03725 D = -2.19626×10^{-6}	A = -0.01393 B = 5.36897×10^{-7} C = 0.02565 D = -1.8752×10^{-5}
$\text{Ge}_{0.1}\text{Se}_{0.2}$	A = -0.01503 B = 2.62617×10^{-5} C = 0.00669 D = -1.94881×10^{-6}	A = -0.000873 B = 2.02143×10^{-7} C = 0.00898 D = -3.47222×10^{-6}	A = -0.00866 B = 1.38891×10^{-6} C = 0.01595 D = -1.31944×10^{-5}	A = -0.01151 B = 7.77451×10^{-6} C = 0.02081 D = -3.44271×10^{-7}	A = -0.00738 B = 4.16667×10^{-6} C = 0.02776 D = -1.73611×10^{-5}

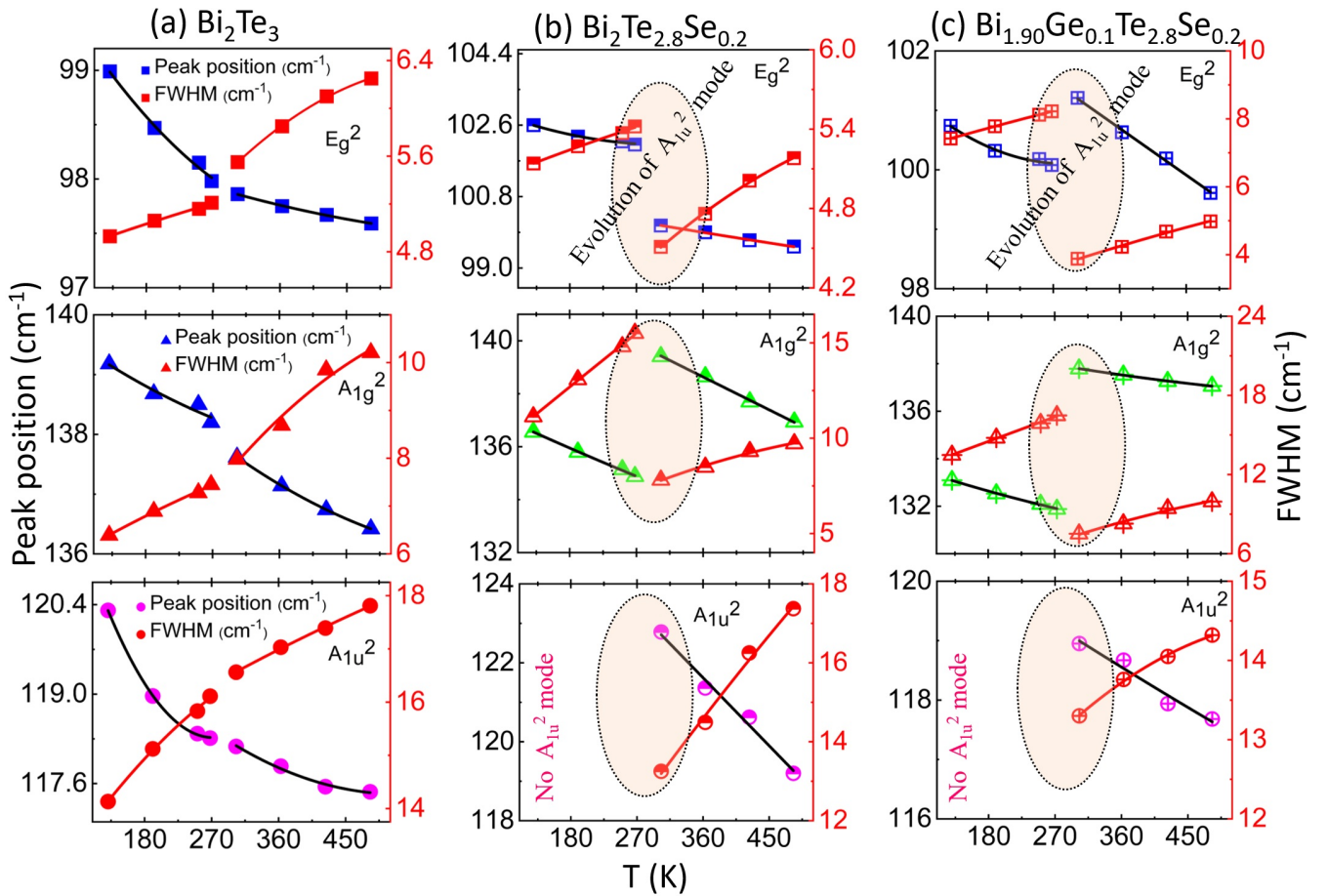


FIG. 7. Variation of peak position and FWHM of E_g^2 , A_{1u}^2 , and A_{1g}^2 phonon modes with temperature from 131 to 483 K for (a) Bi_2Te_3 , (b) $\text{Bi}_2\text{Te}_{2.8}\text{Se}_{0.2}$, and (c) $\text{Bi}_{1.90}\text{Ge}_{0.1}\text{Te}_{2.8}\text{Se}_{0.2}$. The dotted ellipsoidal region in (b) and (c) corresponds to the evolution of A_{1u}^2 at around 278 K in the doped samples. The points represent the measured data points, whereas the line represents the fitting of peak position and FWHM according to Eq. (2) and Eq. (3), respectively.

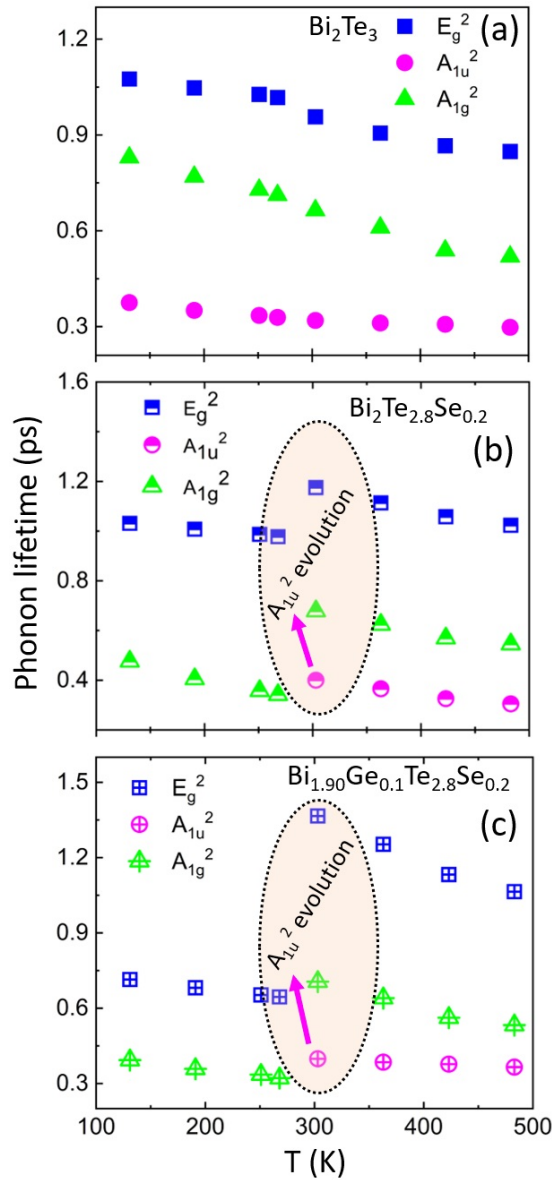


FIG. 8. Estimated phonon lifetime for E_g^2 , A_{1u}^2 , and A_{1g}^2 , with peaks of (a) Bi_2Te_3 , (b) $\text{Bi}_2\text{Te}_{2.8}\text{Se}_{0.2}$, and (c) $\text{Bi}_{1.90}\text{Ge}_{0.1}\text{Te}_{2.8}\text{Se}_{0.2}$ at different temperatures. Since A_{1u}^2 is absent at low temperatures in the doped samples, phonon lifetime corresponding to A_{1u}^2 in doped samples could not be calculated.

simultaneously contribute to the optical phonon decay in the entire temperature range studied here. Accordingly, the temperature dependent phonon frequency (ω) and FWHM (Γ) can be written as [20,33–36]

$$\omega(T) = \omega_0 + A \left[1 + \frac{2}{e^x - 1} \right] + B \left[1 + \frac{3}{e^y - 1} + \frac{3}{(e^y - 1)^2} \right], \quad (2)$$

$$\Gamma(T) = \Gamma_0 + C \left[1 + \frac{2}{e^x - 1} \right] + D \left[1 + \frac{3}{e^y - 1} + \frac{3}{(e^y - 1)^2} \right]. \quad (3)$$

Here, the x and y can be written as $x = \frac{\hbar c \omega_0}{2k_B T}$ and $y = \frac{\hbar c \omega_0}{3k_B T}$, where ω_0 is the intrinsic frequency of the optical phonon mode and Γ_0 represents the peak broadening due to disorder and boundary scattering. A , B , C , and D are the anharmonic constants. Planck's constant, the speed of light, and the Boltzmann constant are represented by \hbar , c , and k_B , respectively. Both the second and third terms in Eq. (2) and Eq. (3) collectively account for the phonon damping part, which arises due to the anharmonic phonon vibrations and corresponds to the three phonon decay processes (second term) and four phonon decay processes (third term).

The anharmonic constants are obtained from the best fit of the temperature-induced Raman peak shift using Eq. (2) and the temperature evolution of FWHM of Raman peaks to Eq. (3). The best fit together with the measured data corresponding to the temperature window from 131 K to 278 K for doped and undoped samples is shown in Fig. 7. We note that the A_{1u}^2 peak is absent for the doped samples in the low-temperature region; therefore, we have only analyzed the E_g^2 and A_{1g}^2 peaks from the 131 to 283 K temperature region. Similarly, for a temperature window from 300 K to 483 K, the measured data along with the best fit to Eq. (2) and Eq. (3) are shown in Fig. 7. The harmonic constants, i.e., A , B , C , and D , obtained from the best fits in different temperature windows are tabulated in Table II. As can be seen from Table II, the harmonic constants A and D turn out to be negative and B and C are positive for all the samples studied here. This indicates the three phonon decay process is dominant in undoped and doped Bi_2Te_3 systems [17,20]. The anharmonic contribution due to three phonon coupling [$\Delta\omega^{(2)}(T)$ and $\Delta\Gamma^{(2)}(T)$] is estimated from temperature dependent peak shift and FWHM using Klemens's model [33,34,36,37],

$$\Delta\omega^{(2)}(T) = A[1 + n(\omega_1) + n(\omega_2)], \quad (4)$$

$$\Delta\Gamma^{(2)}(T) = C[1 + n(\omega_1) + n(\omega_2)], \quad (5)$$

where $n(\omega) = [e^{(\hbar\omega/k_B T)} - 1]^{-1}$, $\omega_1 = \omega_2 = \omega_0/2$, and ω_0 is the harmonic constant. A and C are the anharmonic constants obtained by fitting the temperature-induced Raman peak shift using Eq. (2) and the temperature evolution of FWHM of Raman peaks to Eq. (3). The estimated $\Delta\omega^{(2)}(T)$ and $\Delta\Gamma^{(2)}(T)$ values are given in Table S1, and Table S3 for 131 K to 268 K, whereas Table S2 and Table S4 represent the 303 K to 483 K temperature range [38]. It can be clearly observed from Tables S1–S4 [38] that the anharmonic contributions of the Raman modes due to three phonon coupling increase with increase in temperature. The increase in anharmonic contributions with an increase in temperature leads to decay of optical phonons and decrease in lattice thermal conductivity at higher temperatures. The decay of optical phonons reduces the phonon lifetime in doped and undoped samples. Where $n(\omega) = [e^{(\hbar\omega/k_B T)} - 1]^{-1}$, $\omega_1 = \omega_2 = \omega_0/2$, and ω_0 is the harmonic constant. A and C are the anharmonic constants obtained by fitting the temperature-induced Raman peak shift using Eq. (2) and the temperature evolution of FWHM of Raman peaks to Eq. (3). The estimated $\Delta\omega^{(2)}(T)$ and $\Delta\Gamma^{(2)}(T)$ values are given in Table S1 and Table S3 for 131 K to 268 K, whereas Table S2 and Table S4 represent

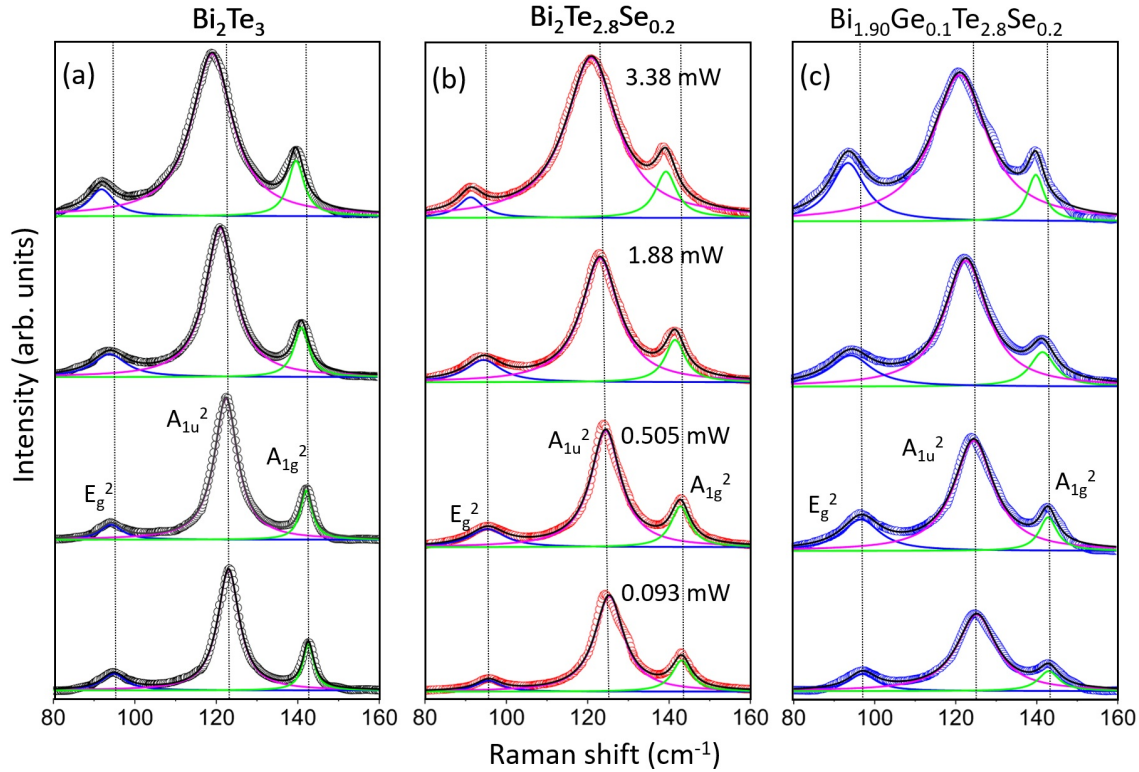


FIG. 9. Raman spectra collected at varying laser power for (a) Bi_2Te_3 , (b) $\text{Bi}_2\text{Te}_{2.8}\text{Se}_{0.2}$, and (c) $\text{Bi}_{1.90}\text{Ge}_{0.1}\text{Te}_{2.8}\text{Se}_{0.2}$.

the 303 K to 483 K temperature range. It can be clearly observed from Tables S1–S4 [38] that the anharmonic contributions of the Raman modes due to three phonon coupling increase with increase in temperature. The increase in anharmonic contributions with an increase in temperature leads to decay of optical phonons and decrease in lattice thermal conductivity at higher temperatures. The decay of optical phonons reduces the phonon lifetime in doped and undoped samples.

Next, we estimate the optical phonon lifetime of three optical modes (E_g^2 , A_{1u}^2 , and A_{1g}^2) for undoped and doped samples in the temperature range of 131–483 K using the relation [39] $\frac{\Gamma}{\hbar} = \frac{1}{\tau}$, where Γ is the FWHM in cm^{-1} and $\hbar = h/2\pi = 5.3 \times 10^{-12} \text{ cm}^{-1}\text{s}$. The temperature evolution of phonon lifetime for different optical modes is plotted in Figs. 8(a), 8(b) and 8(c). As can be seen from Fig. 8, the phonon lifetime of all-optical phonon modes decreases continuously with an increase in temperature for the binary/undoped Bi_2Te_3 sample. On the contrary, for doped Bi_2Te_3 , an anomaly is observed between 280 and 300 K. The phonon lifetime suddenly increases at around 280 K and decreases thereafter with the increase in temperature. This anomaly is associated with the evolution of A_{1u} peak, which also appears at 280 K. Our studies clearly establish a reduction in phonon lifetime with an increase in temperature, irrespective of the doping state of the sample. Since the phonon lifetime is directly connected with the heat transport in these materials, hence the thermal conductivity is expected to decrease in the temperature range from 130 to 483 K with a small anomaly for the doped samples in the 280–300 K temperature region.

The lattice thermal conductivity is calculated in the undoped and doped Bi_2Te_3 samples by analyzing the temperature-dependent and power-dependent evolution of Raman modes. As the Raman peak shifts are related to the atoms/lattice vibrations induced due to the thermal energy, lattice thermal conductivity (κ_{lattice}) is calculated by considering radial heat flow using the following equation [40]:

$$\kappa = \frac{\frac{\Delta\omega}{\Delta T}}{4\sqrt{\pi}r\frac{\Delta\omega}{\Delta P}}, \quad (6)$$

where “ r ” is known as the radius of the objective aperture and P is the power of the laser light. $\frac{\Delta\omega}{\Delta T}$ and $\frac{\Delta\omega}{\Delta P}$ are known as the temperature and power coefficients, respectively. In this Raman measurement, an objective with $50\times$ magnification is used, which corresponds to an “ r ” value of $\sim 3 \mu\text{m}$. The numerator $\frac{\Delta\omega}{\Delta T}$ of Eq. (6) is obtained from the Raman peak shift with respect to temperature. The shift in Raman peaks with an increase in temperature can be analyzed using the following equation [41]:

$$\omega(T) = \omega_0 + \alpha_1 T + \alpha_2 T^2, \quad (7)$$

where ω_0 is the harmonic frequency and α_1 and α_2 are the first- and second-order temperature coefficients of the Raman modes. The denominator term $\frac{\Delta\omega}{\Delta P}$ is derived from the Raman peak shift to incident laser power. The room-temperature power-dependent Raman spectra for undoped and doped Bi_2Te_3 samples are collected at 0.093, 0.515, 1.88, and 3.38 mW laser power and are shown in Fig. 9. The Raman peak shifts towards lower frequency with an increase in Raman power. The redshift of the Raman peaks to laser power

TABLE III. Values of power coefficient ($\frac{\Delta\omega}{\Delta P}$) evaluated by fitting the power dependent Raman spectroscopy data with Eq. (5) and room temperature κ_{lattice} of Bi_2Te_3 , $\text{Bi}_2\text{Te}_{2.8}\text{Se}_{0.2}$, and $\text{Bi}_{1.90}\text{Ge}_{0.1}\text{Te}_{2.8}\text{Se}_{0.2}$ samples.

Parameters	Bi_2Te_3	$\text{Bi}_2\text{Te}_{2.8}\text{Se}_{0.2}$	$\text{Bi}_{1.90}\text{Ge}_{0.1}\text{Te}_{2.8}\text{Se}_{0.2}$
$(\frac{\Delta\omega}{\Delta P})_{E_g^2}$	-0.8231	-1.17088	-0.97885
$(\frac{\Delta\omega}{\Delta P})_{A_{1u}^2}$	-1.09341	-1.12409	-1.1123
$(\frac{\Delta\omega}{\Delta P})_{A_{1g}^2}$	-0.81373	-1.06423	-0.91369
κ_{lattice} ($\text{W m}^{-1} \text{K}^{-1}$) (estimated from Raman spectroscopy)	0.6014	0.5246	0.3931
κ_{lattice} ($\text{W m}^{-1} \text{K}^{-1}$) (from PPMS measurement)	NA	0.37812	0.4081

can be characterized by the following equation [42,43]:

$$\Delta\omega = \omega P_2 - \omega P_1 = \chi_P(P_2 - P_1) = \chi_P \Delta P, \quad (8)$$

where χ_P is the first-order power-dependent coefficient and ω represents the Raman peak shift of the samples at varying laser power. The power dependent Raman spectra of Bi_2Te_3 , $\text{Bi}_2\text{Te}_{2.8}\text{Se}_{0.2}$, and $\text{Bi}_{1.90}\text{Ge}_{0.01}\text{Te}_{2.8}\text{Se}_{0.2}$ samples are fitted with a linear function shown in Eq. (8). The values of the power coefficients for all Raman modes are listed in Table III. The lattice thermal conductivity of Bi_2Te_3 , $\text{Bi}_2\text{Te}_{2.8}\text{Se}_{0.2}$, and $\text{Bi}_{1.90}\text{Ge}_{0.1}\text{Te}_{2.8}\text{Se}_{0.2}$ samples is calculated using Eq. (4) and is tabulated in Table III. The thermal conductivity κ_{lattice} is found to be more in Se-dge codoped Bi_2Te_3 than that for the Se-doped Bi_2Te_3 . To juxtapose the observed trend in thermal conductivity, the κ is experimentally measured for undoped and doped samples using PPMS. The lattice thermal conductivity (κ_{lattice}) is obtained by subtracting the electronic thermal conductivity (κ_e) from the measured total thermal conductivity [44], i.e., $\kappa_{\text{lattice}} = \kappa - \kappa_e$. We have estimated the electronic contribution to thermal conductivity (κ_e) by using Wiedemann-Franz law $\kappa_e = \frac{LT}{\rho}$, where L is the Lorenz number and ρ is the electrical resistivity of the sample. The value of L is calculated using the equation $L = 1.5 + \exp(-|S|)/116$, where S is the Seebeck coefficient of the sample in $\mu\text{V K}^{-1}$. The unit of L is written in the unit of $10^{-8} \text{W}\Omega \text{K}^{-2}$.

The temperature dependence of electrical resistivity (ρ) and Seebeck coefficient (S) measured for doped and undoped samples is shown in Figs. 10(a) and 10(b). The experimentally measured values of S and ρ are used to estimate the value of κ_e of the samples. The κ for Se-doped Bi_2Te_3 is found to be more than that of the Se-Ge codoped Bi_2Te_3 system [Fig. 10(c)]. Interestingly, κ_{lattice} turns out to be lower in Se-doped Bi_2Te_3 , which is in line with that estimated from the Raman modes (Table III). The higher κ_{lattice} value in the Se-Ge codoped sample as depicted in Fig. 10(d) may be due to the replacement of the heavier ‘‘Bi’’ atom with a lighter ‘‘Ge’’ atom. Also, it is envisaged to observe that the experimentally measured κ_{lattice} values at 300 K match well with that of the calculated values from Raman modes (Table III). Therefore, it may be concluded that lattice thermal conductivity in ternary and quaternary Bi_2Te_3 systems can be estimated from the temperature and power-dependent Raman spectroscopy data. Next, we have fitted the experimentally measured temperature-dependent lattice thermal conductivity data with T^{-x} in the temperature range of 150 K to 312 K to find the effect of various phonon scattering on the κ_{lattice} [5] and the fitted curve

is depicted in Fig. 10(d). It is found that the value of $x \sim 0.87$ and 1.11 for $\text{Bi}_2\text{Te}_{2.98}\text{Se}_{0.2}$ and $\text{Bi}_{1.9}\text{Ge}_{0.1}\text{Te}_{2.98}\text{Se}_{0.2}$ prove the dominant phonon-phonon umklapp scattering in the doped samples [44].

Further, the overall power factor ($\text{PF} = S^2/\rho$) for undoped and doped samples is calculated and plotted in Fig. 10(e). The power factor of the samples is found to increase with temperature. It is observed that the $\text{Bi}_{1.9}\text{Ge}_{0.1}\text{Te}_{2.98}\text{Se}_{0.2}$ sample has higher PF in 312 K and the $\text{Bi}_2\text{Te}_{2.98}\text{Se}_{0.2}$ sample has highest PF from 312 K. Using the value of PF and κ , the thermoelectric figure of merit ($zT = \text{PF} \times T/\kappa$) of the doped samples is evaluated and plotted in Fig. 10(f). It confirms the increase in zT values with increasing temperature and the highest $zT \sim 0.39$ is achieved in Se-Ge codoped $\text{Bi}_2\text{Te}_{2.8}\text{Se}_{0.2}$ at 312 K and remains almost constant afterward. Therefore, it can be stated that the $\text{Bi}_{1.9}\text{Ge}_{0.1}\text{Te}_{2.98}\text{Se}_{0.2}$ sample can be used as an efficient thermoelectric material for near room temperature applications.

IV. SUMMARY AND CONCLUSION

In summary, in-depth investigation of the temperature-dependent Raman spectroscopy for the undoped/binary, Se-doped/ternary, and Se-Ge codoped/quaternary Bi_2Te_3 samples are carried out in the temperature range of 131–483 K, to understand the different optical phonon modes, phonon lifetime, and lattice thermal conductivity in the undoped and doped Bi_2Te_3 . We found that higher bond strength in the doped Bi_2Te_3 could prohibit the inverse symmetry lowering in the low-temperature region and hence the IR-active A_{1u} mode is suppressed in the doped Bi_2Te_3 at a temperature below 270 K. The Raman peaks shift towards a lower wave number and the full width at half maxima of the Raman peaks increases with a rise in temperature, which is confirmed from the temperature-dependent Raman spectroscopy data. The phonon lifetime is found to decrease with an increase in temperature, which is a clear signature of the optical phonon decay at higher temperatures. The estimated lattice thermal conductivity from the optical phonon modes matches well with the experimentally measured values, which confirms that Raman spectroscopy can be used to predict the lattice thermal conductivity of the bulk Bi_2Te_3 based thermoelectric materials. Measurement of thermoelectric properties shows the Ge-Se codoped ternary Bi_2Te_3 having higher thermoelectric properties at 300 K compared to Se-doped ternary Bi_2Te_3 . Our results give an insight into the optical phonon decay mechanism in the doped Bi_2Te_3 and corroborate the

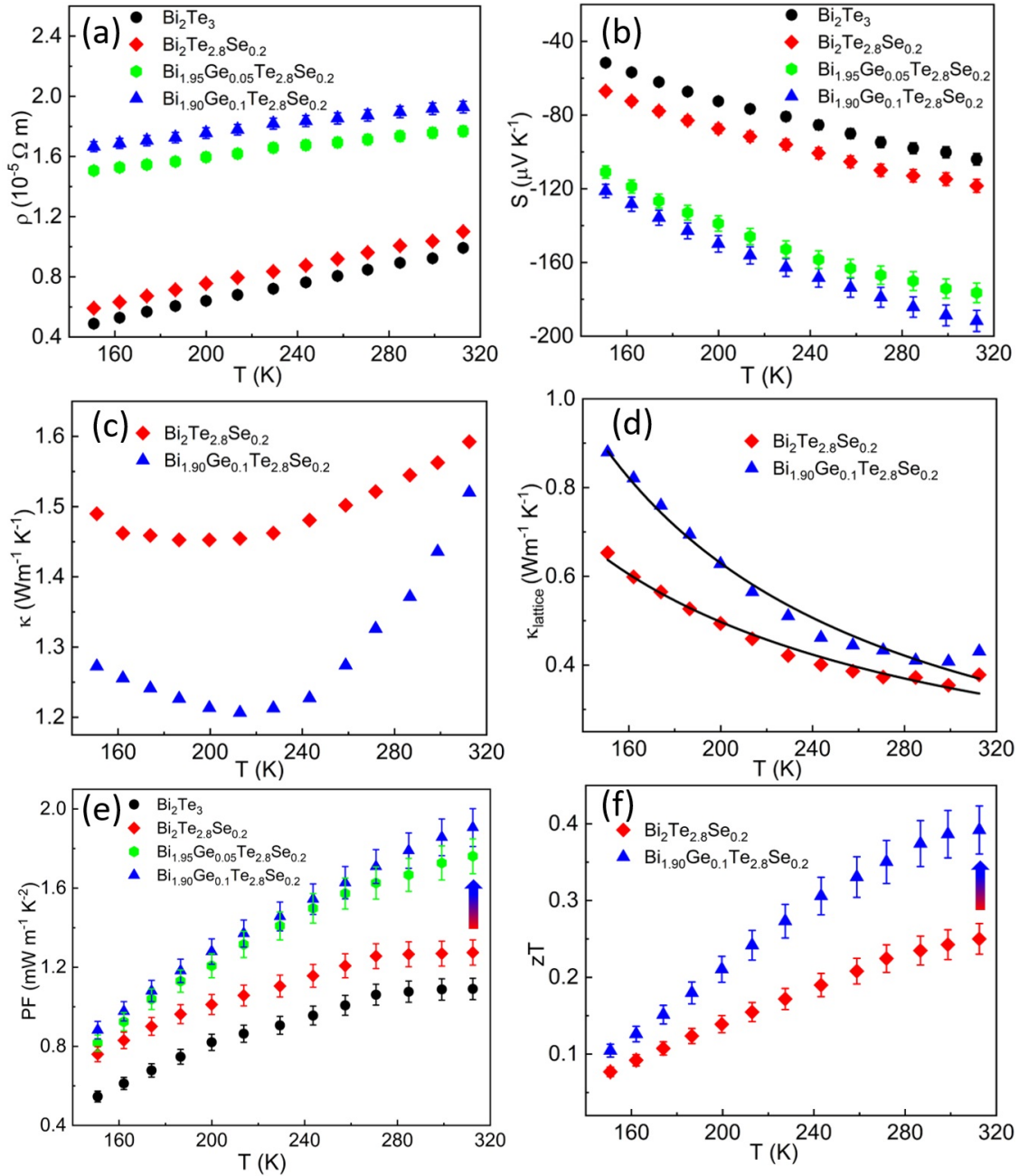


FIG. 10. Temperature variation of (a) electrical resistivity (ρ) and (b) Seebeck coefficient (S) of the investigated samples from 150 to 310 K. Panels (c) and (d) respectively represent the total thermal conductivity and lattice thermal conductivity of $\text{Bi}_2\text{Te}_{2.8}\text{Se}_{0.2}$ and $\text{Bi}_{1.90}\text{Ge}_{0.1}\text{Te}_{2.8}\text{Se}_{0.2}$. The line in (d) shows the fitting of lattice thermal conductivity with T^{-x} . Power factor (PF) and figure of merit (zT) of $\text{Bi}_2\text{Te}_{2.8}\text{Se}_{0.2}$ and $\text{Bi}_{1.90}\text{Ge}_{0.1}\text{Te}_{2.8}\text{Se}_{0.2}$ are depicted in (e) and (f), respectively.

potential of the Se-Ge codoped/quaternary Bi_2Te_3 as efficient thermoelectric materials for near room temperature applications.

ACKNOWLEDGMENT

Financial support from India through IMPRINT-I scheme is acknowledged.

[1] M. S. Dresselhaus, G. Chen, M. Y. Tang, R. Yang, H. Lee, D. Wang, Z. Ren, J.-P. Fleurial, and P. Gogna, New directions for low-dimensional thermoelectric materials, *Adv. Mater.* **19**, 1043 (2007).

[2] G. Snyder and E. Rowe, in *Thermoelectrics Handbook: Macro to Nano*, edited by D. M. Rowe, Thermoelectric Power Generation: Efficiency and Compatibility (CRC Press, New York, 2006).

- [3] L. E. Bell, Cooling, heating, generating power, and recovering waste heat with thermoelectric systems, *Science* **321**, 1457 (2008).
- [4] F. Wu, Q. He, M. Tang, and H. Song, Thermoelectric properties of tl and i dual-doped Bi_2Te_3 -based alloys, *Int. J. Mod. Phys. B* **32**, 1850123 (2018).
- [5] M. Tiadi, M. Battabyal, P. Jain, A. Chauhan, D. K. Satapathy, and R. Gopalan, Enhancing the thermoelectric efficiency in p-type Mg_3Sb_2 via Mg site co-doping, *Sustainable Energy Fuels* **5**, 4104 (2021).
- [6] A. Das, A. Chauhan, V. Trivedi, M. Tiadi, R. Kumar, M. Battabyal, and D. K. Satapathy, Effect of iodine doping on the electrical, thermal and mechanical properties of SnSe for thermoelectric applications, *Phys. Chem. Chem. Phys.* **23**, 4230 (2021).
- [7] V. Trivedi, M. Battabyal, P. Balasubramanian, G. M. Muralikrishna, P. K. Jain, and R. Gopalan, Microstructure and doping effect on the enhancement of the thermoelectric properties of Ni doped Dy filled CoSb_3 skutterudites, *Sustainable Energy Fuels* **2**, 2687 (2018).
- [8] M. Battabyal, B. Priyadarshini, D. Sivaprahasam, N. Karthiselva, and R. Gopalan, The effect of Cu_2O nanoparticle dispersion on the thermoelectric properties of n-type skutterudites, *J. Phys. D* **48**, 455309 (2015).
- [9] H. Zhang, C.-X. Liu, X.-L. Qi, X. Dai, Z. Fang, and S.-C. Zhang, Topological insulators in Bi_2Se_3 , Bi_2Te_3 and Sb_2Te_3 with a single dirac cone on the surface, *Nat. Phys.* **5**, 438 (2009).
- [10] Y. Liang, W. Wang, B. Zeng, G. Zhang, J. Huang, J. Li, T. Li, Y. Song, and X. Zhang, Raman scattering investigation of Bi_2Te_3 hexagonal nanoplates prepared by a solvothermal process in the absence of naoh, *J. Alloys Compd.* **509**, 5147 (2011).
- [11] B. Poudel, Q. Hao, Y. Ma, Y. Lan, A. Minnich, B. Yu, X. Yan, D. Wang, A. Muto, D. Vashaee *et al.*, High-thermoelectric performance of nanostructured bismuth antimony telluride bulk alloys, *Science* **320**, 634 (2008).
- [12] Y. Yu, Z. Wu, O. Cojocaru-Mirédin, B. Zhu, X.-Y. Wang, N. Gao, Z.-Y. Huang, and F.-Q. Zu, Dependence of solidification for $\text{Bi}_2\text{Te}_{3-x}\text{Se}_x$ alloys on their liquid states, *Sci. Rep.* **7**, 2463 (2017).
- [13] Z. Ren, A. A. Taskin, S. Sasaki, K. Segawa, and Y. Ando, Large bulk resistivity and surface quantum oscillations in the topological insulator BiSbTeSe_2 , *Phys. Rev. B* **82**, 241306(R) (2010).
- [14] Y. Xu, I. Miotkowski, C. Liu, J. Tian, H. Nam, N. Alidoust, J. Hu, C.-K. Shih, M. Z. Hasan, and Y. P. Chen, Observation of topological surface state quantum hall effect in an intrinsic three-dimensional topological insulator, *Nat. Phys.* **10**, 956 (2014).
- [15] F. Yang, S. Ghatak, A. A. Taskin, K. Segawa, Y. Ando, M. Shiraishi, Y. Kanai, K. Matsumoto, A. Rosch, and Y. Ando, Switching of charge-current-induced spin polarization in the topological insulator BiSbTeSe_2 , *Phys. Rev. B* **94**, 075304 (2016).
- [16] B.-L. Huang and M. Kaviani, Ab initio and molecular dynamics predictions for electron and phonon transport in bismuth telluride, *Phys. Rev. B* **77**, 125209 (2008).
- [17] S. Kumar, M. Battabyal, K. Sethupathi, and D. K. Satapathy, Thermoelectric properties of Ag-doped CuI: A temperature dependent optical phonon study, *Phys. Chem. Chem. Phys.* **24**, 24228 (2022).
- [18] M. Battabyal, B. Priyadarshini, L. Pradipkanti, D. K. Satapathy, and R. Gopalan, Phase stability and lattice thermal conductivity reduction in CoSb_3 skutterudites, doped with chalcogen atoms, *AIP Adv.* **6**, 075308 (2016).
- [19] J. Zhang, Z. Peng, A. Soni, Y. Zhao, Y. Xiong, B. Peng, J. Wang, M. S. Dresselhaus, and Q. Xiong, Raman spectroscopy of few-quintuple layer topological insulator Bi_2Se_3 nanoplatelets, *Nano Lett.* **11**, 2407 (2011).
- [20] H. He and Z. Zhang, Decay mechanism of optical phonons in γ -cui, *AIP Adv.* **9**, 055104 (2019).
- [21] J. Jenkins, J. Rayne, and R. Ure, Jr., Elastic moduli and phonon properties of Bi_2Te_3 , *Phys. Rev. B* **5**, 3171 (1972).
- [22] J. Zhang, L. Song, S. H. Pedersen, H. Yin, L. T. Hung, and B. B. Iversen, Discovery of high-performance low-cost n-type Mg_3Sb_2 -based thermoelectric materials with multi-valley conduction bands, *Nat. Commun.* **8**, 13901 (2017).
- [23] Y. Selivanov, V. Martovitskii, M. Bannikov, and A. Kuntsevich, Sr., Effect of Sr doping on structural and transport properties of Bi_2Te_3 , *Materials* **14**, 7528 (2021).
- [24] D. Bessas, I. Sergueev, H.-C. Wille, J. PerBon, D. Ebling, and R. P. Hermann, Lattice dynamics in Bi_2Te_3 and Sb_2Te_3 : Te and Sb density of phonon states, *Phys. Rev. B* **86**, 224301 (2012).
- [25] K. Shahil, M. Hossain, D. Teweldebrhan, and A. Balandin, Crystal symmetry breaking in few-quintuple Bi_2Te_3 films: Applications in nanometrology of topological insulators, *Appl. Phys. Lett.* **96**, 153103 (2010).
- [26] R. German, E. V. Komleva, P. Stein, V. G. Mazurenko, Z. Wang, S. V. Streltsov, Y. Ando, and P. H. M. van Loosdrecht, Phonon mode calculations and Raman spectroscopy of the bulk-insulating topological insulator BiSbTeSe_2 , *Phys. Rev. Mater.* **3**, 054204 (2019).
- [27] K. Shahil, M. Hossain, V. Goyal, and A. Balandin, Micro-Raman spectroscopy of mechanically exfoliated few-quintuple layers of Bi_2Te_3 , Bi_2Se_3 , and Sb_2Te_3 materials, *J. Appl. Phys.* **111**, 054305 (2012).
- [28] Y. Peter and M. Cardona, *Fundamentals of Semiconductors: Physics and Materials Properties* (Springer Science & Business Media, New York, 2010).
- [29] W. Richter and C. Becker, A Raman and far-infrared investigation of phonons in the rhombohedral v_2 - v_3 compounds Bi_2Te_3 , Bi_2Se_3 , Sb_2Te_3 and $\text{Bi}_2(\text{Te}_{1-x}\text{Se}_x)_3$ ($0 < x < 1$), $(\text{Bi}_{1-y}\text{Sb}_y)_2\text{Te}_3$ ($0 < y < 1$), *Phys. Status Solidi B* **84**, 619 (1977).
- [30] F. Liu, M. Karakaya, P. Puneet, R. Rao, R. Podila, S. Bhattacharya, and A. Rao, A micro-Raman study of exfoliated few-layered n-type $\text{Bi}_2\text{Te}_{2.7}\text{Se}_{0.3}$, *Sci. Rep.* **7**, 16535 (2017).
- [31] P. Singha, S. Das, V. Kulbachinskii, V. Kytin, A. Apreleva, D. Voneshen, T. Guidi, A. V. Powell, S. Chatterjee, A. Deb, S. Bandyopadhyay, and A. Banerjee, Evidence of improvement in thermoelectric parameters of n-type Bi_2Te_3 /graphite nanocomposite, *J. Appl. Phys.* **129**, 055108 (2021).
- [32] L. M. Pavlova, Y. I. Shtern, and R. E. Mironov, Thermal expansion of bismuth telluride, *High Temp.* **49**, 369 (2011).
- [33] Y. Tian, G. B. Osterhoudt, S. Jia, R. J. Cava, and K. S. Burch, Local phonon mode in thermoelectric $\text{Bi}_2\text{Te}_2\text{Se}$ from charge neutral antisites, *Appl. Phys. Lett.* **108**, 041911 (2016).

- [34] Y. Tian, S. Jia, R. J. Cava, R. Zhong, J. Schneeloch, G. Gu, and K. S. Burch, Understanding the evolution of anomalous anharmonicity in $\text{Bi}_2\text{Te}_{3-x}\text{Se}_x$, *Phys. Rev. B* **95**, 094104 (2017).
- [35] F. Liu, P. Parajuli, R. Rao, P. C. Wei, A. Karunaratne, S. Bhattacharya, R. Podila, J. He, B. Maruyama, G. Priyadarshan, J. R. Gladden, Y. Y. Chen, and A. M. Rao, Phonon anharmonicity in single-crystalline SnSe, *Phys. Rev. B* **98**, 224309 (2018).
- [36] D. Das, S. Das, P. Singha, K. Malik, A. K. Deb, A. Bhattacharyya, V. A. Kulbachinskii, R. Basu, S. Dhara, S. Bandyopadhyay, and A. Banerjee, Evolution of phonon anharmonicity in Se-doped $\text{Sb}_2\text{Te}_3\text{Sb}_2\text{Te}_3$ thermoelectrics, *Phys. Rev. B* **96**, 064116 (2017).
- [37] P. Klemens, Anharmonic decay of optical phonons, *Phys. Rev.* **148**, 845 (1966).
- [38] See Supplemental Material at <http://link.aps.org/supplemental/10.1103/PhysRevMaterials.7.015401> for anharmonic phonon-phonon coupling terms.
- [39] L. Bergman, D. Alexson, P. L. Murphy, R. J. Nemanich, M. Dutta, M. A. Stroschio, C. Balkas, H. Shin, and R. F. Davis, Raman analysis of phonon lifetimes in AlN and GaN of wurtzite structure, *Phys. Rev. B* **59**, 12977 (1999).
- [40] P. Xiao, E. Chavez-Angel, S. Chaitoglou, M. Sledzinska, A. Dimoulas, C. M. Sotomayor Torres, and A. El Sachat, Anisotropic thermal conductivity of crystalline layered SnSe_2 , *Nano Lett.* **21**, 9172 (2021).
- [41] D. Park, S. Park, K. Jeong, H.-S. Jeong, J. Y. Song, and M.-H. Cho, Thermal and electrical conduction of single-crystal Bi_2Te_3 nanostructures grown using a one step process, *Sci. Rep.* **6**, 19132 (2016).
- [42] R. Yan, J. R. Simpson, S. Bertolazzi, J. Brivio, M. Watson, X. Wu, A. Kis, T. Luo, A. R. Hight Walker, and H. G. Xing, Thermal conductivity of monolayer molybdenum disulfide obtained from temperature-dependent raman spectroscopy, *ACS Nano* **8**, 986 (2014).
- [43] X. Gong, Y. Wang, Q. Hong, J. Liu, C. Yang, H. Zou, Y. Zhou, D. Huang, H. Wu, Z. Zhou *et al.*, In-situ micro-raman study of SnSe single crystals under atmosphere: Effect of laser power and temperature, *Spectrochim. Acta, Part A* **265**, 120375 (2022).
- [44] E. S. Toberer, A. Zevalkink, and G. J. Snyder, Phonon engineering through crystal chemistry, *J. Mater. Chem.* **21**, 15843 (2011).